ACS Catalysis

Research Article

pubs.acs.org/acscatalysis

DFT Study of Oxygen Reduction Reaction on Os/Pt Core−Shell Catalysts Validated by Electrochemical Experiment

Ho-Cheng Tsai,[†] Yu-Chi Hsieh,[‡,§] Ted H. Yu,[†,∥] Yi-Juei Lee,[§] Yue-Han Wu,[§] Boris V. Merinov,*[,†] Pu-Wei Wu,[§] San-Yuan Chen,[§] Radoslav R. Adzic,[‡] and William A. Goddard, III*[,†]

[†]Materials and Process Simulation Center (M/C 139-74), California Institute of Technology, 1200 East California Boulevard, Pasadena, California 91125, United States

[‡]Chemistry Department, Brookhaven National Laboratory, Upton, New York 11973, United States

[§]Department of Materials Science and Engineering, National Chiao Tung University, Hsin-Chu 300, Taiwan ROC

[∥]Department of Chemical Engineering, California State University, Long Beach, California 90840, United States

Supporting Information

ABSTRACT: Proton exchange membrane fuel cells (PEMFCs) have attracted much attention as an alternative source of energy with a number of advantages, including high efficiency, sustainability, and environmentally friendly operation. However, the low kinetics of the oxygen reduction reaction (ORR) restricts the performance of PEMFCs. Various types of catalysts have been developed to improve the ORR efficiency, but this problem still needs further investigations and improvements. In this paper, we propose advanced Os/Pt core−shell catalysts based on our previous study on segregation of both bare surfaces and surfaces exposed to ORR adsorbates, and we evaluate the catalytic activity of the proposed materials by density functional theory (DFT). Quantum mechanics was applied to calculate binding energies of ORR species and reaction energy barriers on Os/Pt core−shell catalysts. Our calculations predict a much better catalytic activity of the Os/Pt system than that of pure Pt. We find that the ligand effect of the Os substrate is more important than the lattice compression strain effect. To validate our DFT prediction, we demonstrate the fabrication of Os/Pt core−shell nanoparticles using the underpotential deposition (UPD) technique and succeeding galvanic displacement reaction between the Pt ions and Cu-coated Os nanoparticles. The Os/Pt/C samples were evaluated for electrocatalytic activities toward the ORR in acidic electrolytes. The samples with two consecutive UPD-displacement reaction cycles show 3.5 to 5 times better ORR activities as compared to those of commercially available Pt/C. Our results show good agreement between the computational predictions and electrochemical experimental data for the Os/Pt core−shell ORR catalysts.

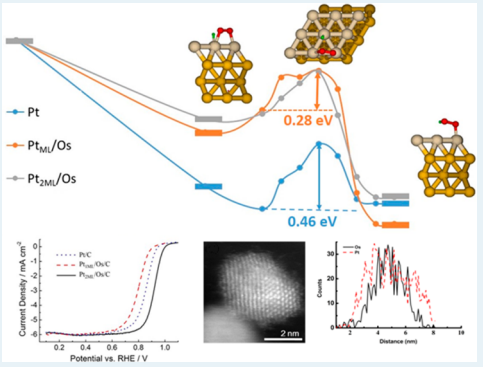

KEYWORDS: *PtOs, core−shell catalysts, DFT, ORR, UPD, electrocatalysis*

1. INTRODUCTION

A proton exchange membrane fuel cell (PEMFC) is considered as a potential technology for automotive applications, stationary/portable power supply, and as a component of hybrid energy systems[1−4] due to its low pollution emission and high efficiency advantages than currently used petroleum-based energy production.[1,2,5] However, the PEMFC performance is limited by the sluggish oxygen reduction reaction (ORR) at the cathode,[6−8] which is much slower and more complicated than the hydrogen oxidation reaction (HOR) at the anode.[8]

ORR mechanisms and electronic structures of ORR catalysts are widely discussed in the literature. For example, Hammer and Nørskov discussed the surface catalysis by considering the interaction between local density of states of adsorbates and d-bands of surfaces.[9] Similar d-band center theory was used by Xin et al. to screen potential alloy catalysts for ORR.[10,11] Holewinski and Linic applied density functional theory (DFT) to simulate the OH/H_2O surface coverage and explained the deviation from ideal Tafel kinetics by microkinetic modeling.[12] Similar microkinetic modeling starting with surface coverage was used to calculate the ORR mechanism and Tafel kinetics for Pt,[13] as well as the surface corrosion and kinetic for Au-modified Pt system.[14,15] Jacob et al. considered current theoretical methods for surface reaction simulations and performed DFT calculation to elucidate the complex ORR mechanism by different pathways.[16,17]

Various types of cathode catalysts, including Pt-based alloys and nonprecious metal catalysts, have been studied widely in the past few years to improve the ORR efficiency and reduce the catalyst cost.[2,18−21] To achieve the desirable high activity, low cost, and durability, new advanced ORR catalyst design approaches are required.[22] In recent years, core−shell and

Received: July 16, 2014
Revised: January 15, 2015
Published: January 22, 2015

DOI: 10.1021/cs501020a
ACS Catal. 2015, 5, 1568−1580

core−shell-like structures of Pt-based alloys have attracted significant attention due to their much better catalytic activity than pure Pt.[23−42] For example, Yang et al. reported that Ru/Pt core−shell catalyst has ∼4 times better activity than pure Pt.[39] The combined experimental and theoretical work of Fribel et al. compared H_{ad} and O/OH_{ad} adsorption on 2D and 3D Pt/Rh(111) surfaces and found that the $H/O/OH_{ad}$ are destabilized in the smooth 2D structure because of the ligand/strain effect of the Rh substrate. However, the geometry effect (both the higher thickness and more defects) balanced the stain/ligand effect and increased the H/O/OH adsorption for the 3D structure derived from the wetting process.[41] Brimaud et al. analyzed the surface character and compared the ORR activity of $Pt_{x\text{-ML}}/Ru(0001)$ and $Pt_xRu_{1-x}/Ru(0001)$ with Pt(111) and found that their ORR activity could exceed the pure Pt ORR activity by modifying the Pt surface content of the $Pt_xRu_{1-x}/Ru(0001)$ alloy or adjusting the thickness of the Pt film to the thickness of $Pt_{x\text{-ML}}/Ru(0001)$.[40] Jackson et al. used core−shell Ru/Pt as an example to prove the feasibility of improving the activity by tailoring the nanostructure.[42] In our previous study,[36] some Pt_3X catalysts, where X is a transition metal, show Pt segregation with formation of so-called Pt-skin on the surface, which improves the catalytic activity of these materials compared to pure Pt.[27] However, it was reported that the components of Pt alloys would be dissolved into electrolyte at the PEMFC operation environment,[43,44] which helps forming the Pt-skeleton structure,[45,46] but could possibly deteriorate because of Ostwald ripening or diffusion.[43−46] This would result in decreased activity of the catalysts.[44,47−49]

Stabilities of Pt-alloys have been studied by different theoretical and experimental methods. For instance, Ma et al.[50] and Chen et al.[51] carried out DFT studies of the Pt_3M alloy surface segregation similar to our work.[52] Wei et al.[53] evaluated the Pt_xMo alloy stability using DFT to calculate the Gibbs free energy change of the surface corrosion. Nørskov and coauthors[28,54] computed the heat of formation to evaluate the stability of Pt-alloys and verified the stability of Pt_3Y and Pt_3Sc by experiment. The same concept was applied by Hwang et al.[55] to explain the experimental results on stability of Pt_3M (M═Y, Zr, Ti, Ni, and Co). Dai et al.[56] combined surface segregation, heat of formation, and d-band center shift calculations to show that PtW alloys may have both better activity and superior stability. Pt-skin formed after annealing or Pt-skeleton structures built after acid-treatment or oxide-leaching after ORR cycling are responsible for the improved catalytic activity and long-term stability of the above-mentioned materials.[57−59]

Our segregation study of Pt_3X alloy bare surfaces[36] indicates that a few alloys show a good segregation energy favoring the Pt-skin formation. However, the situation completely changes, when the surface is exposed to ORR adsorbates, such as O or OH. Only two alloys, Pt_3Ir and Pt_3Os, keep showing the Pt segregation (Pt-skin) in the presence of adsorbed O and OH on the surface[52] (see also Table S1). In poorly segregated alloy surfaces, the non-noble metal component may be or diffuse onto the surface with a risk of leaching out into electrolyte with subsequent degradation of PEMFC performance. To our knowledge, Os and its alloys are rarely studied as ORR catalyst. Most of the literature on Os and its alloys are focused on methanol[60−65] or formic acid[66] oxidation in fuel cell systems. Only $Os_{0.2}Pt_{0.8}/Pd(111)$ was considered as a possible electrocatalyst for ORR,[67] but the corresponding work does not include a complete report. Our earlier performed study demonstrated evidence that proves stability of the Pt-shell structure of dealloyed Pt_2Os.[68] The superior activity and long-term stability allow us to consider the dealloyed Pt_2Os as a potential ORR catalyst. Pt_3Co, Pt_3Ni, and Pt_3Fe alloys are not stable under the fuel cell conditions and leach out into electrolyte,[69,70] which is widely discussed in the literature. This experimental observation is supported by a theoretical study[71] as well.

In this study, we carried out quantum mechanics (QM) calculations on periodic slabs to predict catalytic activity of Os/Pt core−shell catalysts. Perfect hcp (0001) and fcc (111) slabs were applied for Os, Pt, and Pt/Os surfaces. Full kinetic modeling of complex reactions, such as ORR, on nanoparticles still remains a challenge for atomistic first-principles simulations. Although a slab model applied in our calculations is mostly relevant for extended surfaces and neglects natural strain, morphology, or any defects (i.e., edge and kink sites, multiple terraces and corners, and other peculiarities observed in nanoparticles), several fundamental issues of the surface ORR can be analyzed using the methodology applied, because the highly coordinated (111) facets are most conducive to the ORR on small nanoparticles.[30] Although the above-mentioned features of nanoparticles may change binding energies of the ORR intermediates and reaction barriers compared to those on extended surfaces, the slab approach is still sufficient enough for predicting ORR trends. Moreover, reported experimental results indicate that the higher catalytic activity of Pt_3M alloy extended surfaces compared to that of Pt is reproduced qualitatively on surfaces of Pt_3M alloy nanoparticles.[72−77] To validate our theoretical predictions, we used the under potential deposition (UPD) method for the core−shell catalyst fabrication[22,32,72−77] with succeeding analysis of ORR activity of the fabricated Os/Pt core−shell catalysts.

2. METHODOLOGY

Computational. In this study, we apply the DFT method to evaluate the catalytic activity of the Os/Pt core−shell structures and perform electrochemical experiments to confirm our computational prediction.

All calculations were carried out using the SeqQuest code[78] with the Perdew−Burke−Ernzerhof (PBE) functional[79] in the generalized gradient approximation (GGA)[80,81] for the periodic QM calculations. Seqquest uses a double-ζ-plus polarization Gaussian basis set rather than a plane wave basis that is used in other DFT codes.

Angular-momentum-projected norm-conserving nonlocal effective core-potentials (pseudopotentials)[82−86] were used to replace the core electrons. The reciprocal space grid is 5 × 5 × 0 for all our slab calculations and 12 × 12 × 12 for our lattice constants calculation. All calculations have been performed with spin-optimization. A 3 × 3 supercell (9 atoms per layer) with 3 to 5 layer Os slabs were used as the core structure. Additional layers of Pt atoms (1−3) on this core structure (the total number of layers in all slabs was 6) were used to simulate the Os/Pt core−shell catalyst structures. In all calculations, we fixed the coordinates of 9 Os atoms in the bottom layer and relax all other atoms in the geometry optimization. For comparison, similar calculations were carried out on 6-layer Pt and Os slabs. The obtained Os−Os and Pt−Pt bond lengths are 2.75 and 2.81 Å, respectively. We used the lowest-energy surfaces in our calculations, the (0001) surface of the hexagonal closed-packed (hcp) structure for Os and the (111) surface of the face-centered cubic (fcc) structure for Pt.

DOI: 10.1021/cs501020a
ACS Catal. 2015, 5, 1568−1580

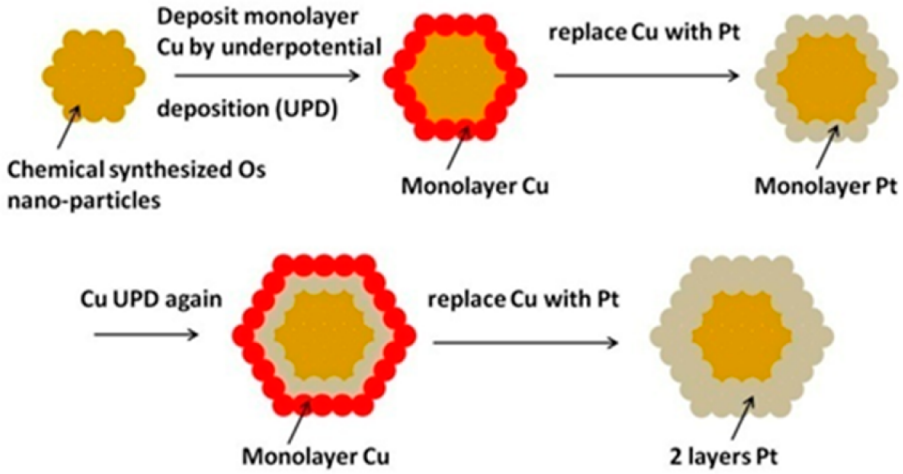

Figure 1. Procedure for Os/Pt core−shell catalyst preparation.

The binding energies are defined as the energy differences between the species adsorbed on the catalyst surface and the sum of the clean catalyst slabs and the species in vacuum:

$$E_{\text{binding}} = E_{\text{MX}} - (E_{\text{M}} + E_{\text{X}})$$

where X is an ORR intermediate and M is a metal.

The reaction energy barriers for each ORR step were calculated using the Nudged Elastic Band (NEB)[87,88] method implemented into the SeqQuest code, and the energy difference between the initial step and the highest NEB image (transition state) was considered as an energy barrier. The initial and final states were determined from the binding energies of the ORR species.

In our calculations, zero point energy (ZPE) and entropy contributions were neglected, because our conclusions about ORR activity are based on the rate-determining step (RDS) barriers, which are energy differences between transition states and initial states. In this case, the above-mentioned contributions may be canceled.

To estimate the solvent effect for the ORR, we used an implicit continuous method[89] with Poisson−Boltzmann approximation.[90−92] In this method, solvation is modeled as the electrostatic interaction between the surface and the aqueous phase. Mulliken populations obtained from the DFT calculations were used for the solvent effect calculations. The solvation energy was then directly added to the DFT gaseous enthalpy as a corrected term.

EXPERIMENTAL SECTION

Os Synthesis. Carbon-supported Os nanoparticles (Os/C) were prepared in a chemical reduction route. First, 50 mg of carbon powders (Ketjen Black) and 19.5 mg of $OsCl_3$ were mixed in 100 mL of ethanol at 25 °C. Next, the temperature of the mixture was raised to 110 °C for 2 h to reach a uniform dispersion. Subsequently, 2.63 mL of 100 mM aqueous KOH solution was added. The mixture underwent further stirring for 30 min and cooled to 25 °C to filter out the Os/C. The dried Os/C was subjected to a reduction treatment at 450 °C for 1 h in an atmosphere of 15% H_2 and 85% Ar. The effective metal loading of the Os nanoparticles was 20 wt % of the Os/C sample.

Preparation of Os/Pt Core−Shell Nanoparticles. We used the UPD method to prepare Os/Pt core−shell nanoparticles. In this method, a monolayer of a sacrificial metal is deposited on the substrate at a potential which is more positive than the reduction potential. Then a more noble metal substitutes the sacrificial metal using galvanic displacement.

Five milligrams of Os/C powders underwent an ultrasonication mixing for 5 min in a solution containing 5 mL of ethanol and 1 μL of 5 wt % Nafion ionomer solution (Sigma-Aldrich) to render homogeneous ink dispersion. Next, 15 μL of the ink dispersion was deposited on a glassy-carbon rotation disk electrode (RDE) serving as a working electrode (Pine Research, electrode diameter is 5 mm and the electrode area is 0.1963 cm^2). Subsequently, the working electrode was immersed in a deaerated aqueous solution of 50 mM $CuSO_4$ and 50 mM H_2SO_4 for 20 cyclic voltammetry (CV) scans with a scan rate of 20 mV/s in a potential window of 0.31 and 0.9 V (vs RHE). The purpose for these CV scans was to precondition the sample and identify the suitable potential for the Cu UPD process. Afterward, a Cu UPD was imposed in which the potential was kept at 0.35 V to allow the Cu to deposit onto the surface of the Os nanoparticles as a monolayered film. Once the depositing current was subdued and stabilized, the sample was removed from the Cu plating solution and immersed immediately to a deaerated aqueous solution containing 1 mM K_2PtCl_4 and 50 mM H_2SO_4. At this stage, a displacement reaction took place in which the Cu atoms on the Os surface were oxidatively dissolved, whereas the Pt ions in the electrolyte were reduced and deposited onto the Os nanoparticles. The sample undergoing a single Cu-UPD/displacement reaction cycle was labeled as Pt_{1ML}/Os/C, and the sample undergoing consecutive Cu-UPD/displacement reaction cycles was labeled as Pt_{2ML}/Os/C. We should emphasize here that Pt_{1ML}/Os/C does not equally mean a completely perfect Pt monolayer deposited on the Os substrate; more details were reported in the Results and Discussion section. The Os/Pt core−shell catalysts production procedure is summarized in Figure 1.

To determine the electrochemically active surface area (ECSA), multiple CV scans were imposed between 0.05 and 1.0 V (vs RHE) at 20 mV/s in a 50 mL of deaerated 0.1 M aqueous $HClO_4$ solution. The Coulomb charge associated with the hydrogen adsorption was integrated and divided by 210 $\mu C\ cm_{Pt}^{-2}$ to obtain the ECSA value for the Pt/C, Pt_{1ML}/Os/C, and Pt_{2ML}/Os/C, respectively. To explore the electrocatalytic

DOI: 10.1021/cs501020a
ACS Catal. 2015, 5, 1568−1580

activities for the ORR, CV scans between 0.1 and 1.05 V (vs RHE) were performed at 20 mV/s in 50 mL of 0.1 M aqueous $HClO_4$ solution. Prior to the ORR experiments, the $HClO_4$ aqueous solution was bubbled with oxygen for 30 min to ensure it was fully saturated with the oxygen. The electrochemical synthesis and ORR measurements were performed at 25 °C in a three-electrode arrangement using a Solartron 1287A electrochemical interface. Ag/AgCl and Pt foils (15 cm^2) were used as the reference and counter electrodes, respectively. In our figures, all potentials were plotted against the RHE. Lastly, identical electrochemical tests were performed on commercially available carbon-supported Pt (Pt/C; 20 wt % Pt on Vulcan XC72R, BASF) for comparison purposes.

Characterization of Materials. A high-resolution transmission electron microscope (HRTEM; JEOL JEM3000F) and high-angle angular dark field (HAADF) technique were employed to observe the morphologies, sizes, and distributions of the Os nanoparticles. The structures and composition profiles of Pt_{1ML}/Os/C and Pt_{2ML}/Os/C were obtained using a JEOL spherical aberration corrected scanning transmission electron microscope (ARM 200F) with an Oxford energy dispersive spectrometer (EDS) in which the Lα and Mα signals from the EDS were recorded to determine the spatial distribution of the Pt and Os atoms. The exact Pt amount in our samples was determined using an inductively coupled plasma mass spectrometer (ICP-MS; Agilent 7500ce).

3. RESULTS AND DISCUSSION

3.1. Stability of the Os/Pt Core−Shell Structure. The crystal structure of Os is hcp, while that of Pt is fcc. The stacking sequences for the closest packed planes of hcp (0001) and fcc (111) are ABABAB and ABCABC, respectively. To determine structures with different numbers of Pt layers deposited on the Os core, we calculated all the stacking sequences and compare their energies (see Table 1). Each letter in the "Pt/Os surface structure" row represents a specific layer in the structure. The capital letters represent Os layers, whereas the lower case denotes Pt layers. For example, the label b/ABA means that the structure has a Pt monolayer with the b stacking on the three Os layer substrate with the ABA stacking sequence. The lowest energy stacking sequence result conforms to the similar DFT result for the Ru(hcp)/Pt(fcc) core−shell catalyst.[39,93] In addition, our recent study using atomic-scale resolution high-angle angular dark field (HAADF) scanning transmission electron microscopy (STEM) technique proves the energetically favorable cb/ABAB stacking sequence for Pt_{2ML}/Ru obtained from the DFT calculation.[93] We used the lowest energy stacking sequences as the stable structures for calculations of binding energies and reaction energy barriers on Pt/Os slabs.

Table 1. Relative Energies (eV) for Pt/Os Surface Structures with Different Stacking Sequences

Pt/Os surface structure	relative energy
Pt_{1ML}/Os	
b/ABA	0.07
c/ABA	**0.00**[a]
Pt_{2ML}/Os	
ab/ABA	0.53
cb/ABA	**0.00**[a]
bc/ABA	0.40
ac/ABA	0.81
Pt_{3ML}/Os	
bab/ABA	0.82
cab/ABA	0.32
acb/ABA	**0.00**[a]
bcb/ABA	0.52
abc/ABA	0.29
cbc/ABA	0.66
bac/ABA	0.64
cac/ABA	1.03

[a]Reference energy: c/ABA: −76283.72 eV; cb/ABA: −99327.96 eV; acb/ABA: −122371.54 eV. All energies are relative to the lowest one (bold numbers).

3.2. Binding Sites and Binding Energies. *Binding Site Notations.* Figure 2 shows the binging sites on Os and Pt/Os surfaces. There are four types of sites on the closed-packing plane:

- On top, bonded to one Os or Pt atom (μ1), denoted as t.
- Bridging between two Os or Pt atom (μ2), denoted as b.
- An fcc position between three Os or Pt atom (μ3), denoted as f.
- An hcp position between three Os or Pt atom (μ3), denoted as h.

In our notations, capital letters represent the binding species, such as H, O, O_2, and so forth. The lower case letters denote the binding sites. For OH and OOH, two and three lower case labels are applied to distinguish the different orientations of the species. Figure 3 illustrates some examples for the labels of OH and OOH species on the Pt/Os catalyst surface. OH/b-f means OH with O adsorbed at the b bridge site and H at the f site. OOH/t-*b*-f denotes OOH with the first O at the top site, the second O at the b bridge site, and the H atom at the f site. OOH/t-f labels only the O positions, the first O at the top site and the second O at the f site. Similar notation rules are applied to other ORR intermediates. Figure 4 shows binding energies of the ORR intermediates at the most stable sites on the Os, Pt, and Pt/Os surfaces in vacuum and solvent. All binding energies for the ORR species at various surface sites are summarized in Tables S2 and S3. It should be noted that after geometry optimization, the OH/f and OH/h spontaneously move to the sites which can be considered as OH/b-f and OH/b-h with similar corresponding energy values.

H Binding. On the pure Os surface, both in gas phase and solvent, H prefers the f site, but the binding energy difference between various sites is not significant.

For Pt and Pt/Os surfaces, the t site is most preferable for the H binding. The binding energy values lie between −2.45 and −2.81 eV in gas phase and −2.61 and −2.90 eV in solvation phase. It is worthwhile to notice that the binding energy rises with an increasing number of deposited Pt layers and approaches the binding energy for the pure Pt surface. A similar trend is observed for most of the ORR species.

O Binding. On the pure Os surface, O binds stronger than on the Pt or Pt/Os surfaces. The binding energy on the Os surface is −5.21 eV at the h site and ranges from −3.16 to −3.68 eV at the f site for Pt and Pt/Os.

In solvation phase, the most stable binding sites are the same as in gas phase. The differences between the O binding energy values on the Os and Pt, Pt/Os surfaces are smaller.

OH Binding. In gas phase, the most stable OH binding site on the Os and Pt surfaces is the b site, whereas the t site is most stable for the Pt/Os surfaces. The binding energy on the Os

DOI: 10.1021/cs501020a
ACS Catal. 2015, 5, 1568−1580

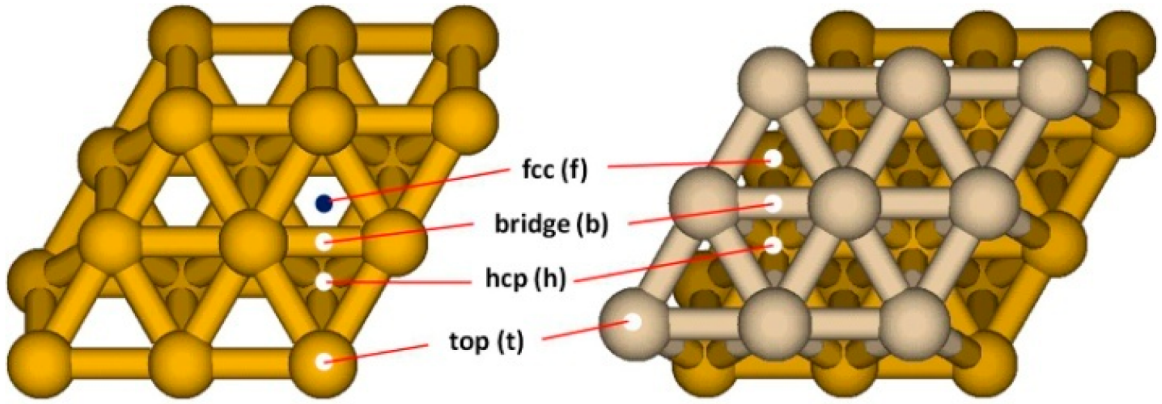

Figure 2. Binding sites on Os (left) and Pt/Os (right) slab surfaces.

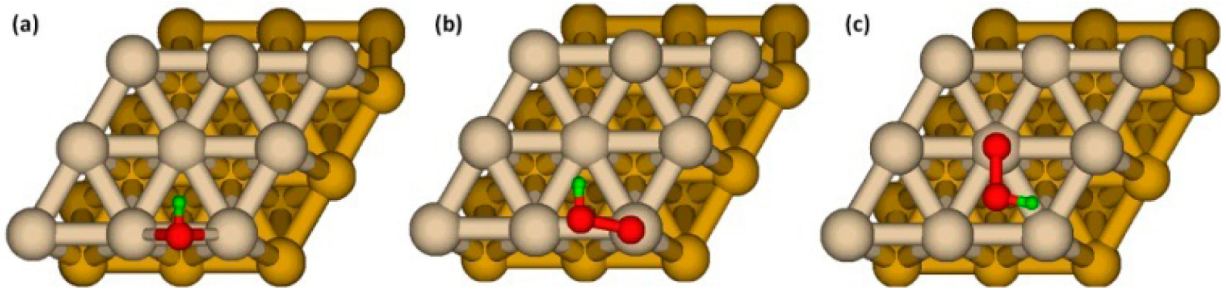

Figure 3. OH and OOH species on the Pt/Os catalyst surface: (a) OH/b-f (b) OOH/t-b-f and (c) OOH/t-f.

surface in gas phase is −3.24 eV, which is lower than −2.31 and −2.21 to −2.29 eV for the Pt and Pt/Os surfaces, respectively. Interestingly, for all catalysts, OH shows no significant binding site preference in gas phase, unlike the solvation phase where the t site is clearly preferable.

In solvation phase, the t site is most stable for all catalysts. The OH binding energy for the Pt_{1ML}/Os is −3.10 eV, higher than on the Os surface (−3.72 eV) but lower than on the Pt surface (−2.83 eV). The OH binding energy does not exhibit an obvious trend versus different numbers of deposited Pt layers, the values vary from −2.80 to −3.10 eV.

O_2 Binding. We use the center of the O−O bond to denote the binding sites of O_2. Thus, the O_2/b means that two O atoms are located approximately on the top of the surface Os or Pt atoms with the O−O bond center at the b site. The O_2/f and O_2/h binding sites are defined as one O atom located on the top of the Os or Pt atom, and the other at the b site with the O−O bond center at the f or h site, respectively. The O_2 binding on the Os surface is stronger than on the Pt and Pt/Os surfaces both in gas phase and solution. The bridge site is most stable for the O_2 adsorption on all surfaces, except for the Os surface in gas phase, where O_2 binds most strongly at the h site.

We find that the O_2 binding energy differences for the b and f sites on Pt_{2ML}/Os and Pt_{3ML}/Os surfaces are as small as 0.02 eV in solvent, which means that during the ORR process, O_2 can probably be adsorbed at both sites. It was also found that the O_2 binding energy for the Pt_{2ML}/Os catalyst is higher than the O_2 binding energy for the Pt_{1ML}/Os and Pt_{3ML}/Os catalysts. The reason for this violation of the expected linear trend is not clear yet.

OOH Binding. For notations of the OOH binding sites, we used two or three letters. The first letter denotes a position of the first oxygen atom, the second letter denotes a position of the second oxygen atom, and the third letter denotes a position of the hydrogen atom. For example, OOH/t-*b*-f means that the first oxygen is located on the top of Pt or Os atom, the second oxygen atom is at the b site (actually, it is between the top and bridge sites), and the hydrogen is at the f site (see Figure 3b). For OOH/t-f or OOH/t-h, the symmetry makes the O−H bond toward right or left to be the same, and therefore, only two letters can be used to denote positions of the two oxygen atoms (see Figure 3c). For the OOH binding on the Os surface in gas and solvation phases, the OOH/t-*b*-f and OOH/t-*b*-h sites are both unstable and OOH spontaneously decomposes into O and OH at the top sites. We find that the OOH binding for the Pt_{2ML}/Os catalyst is weaker than that for the Pt_{1ML}/Os and Pt_{3ML}/Os catalysts, similar to the O_2 binding case.

HOOH and HOH Binding. There is only one site for the HOOH binding: the two O atoms bind to two neighboring Pt atoms similar to the O_2/b case with the O−O bond parallel to the surface Pt−Pt bond. For the HOH binding, the O atom binds at the top site with the two O−H bonds parallel to the surfaces. For the HOH-down binding, one H atom binds at the top site with the remaining O−H bond almost parallel to the surface. The HOOH and HOH binding energies both in gas and solvation phases fit the general trend described before; that is, the binding energies rise with the increasing number of deposited Pt layers and approaches the binding energies for the pure Pt surface. Furthermore, the corresponding binding energies on the Os and Pt_{3ML}/Os surfaces are lower than on the pure Pt surface.

In summary, we can say that the binding on the Os surface is stronger than on the Pt or Pt/Os surfaces in gas and solvated phases. The general trend both in gas phase and solution is that the binding becomes stronger when the number of deposited Pt layers increases.

DOI: 10.1021/cs501020a
ACS Catal. 2015, 5, 1568−1580

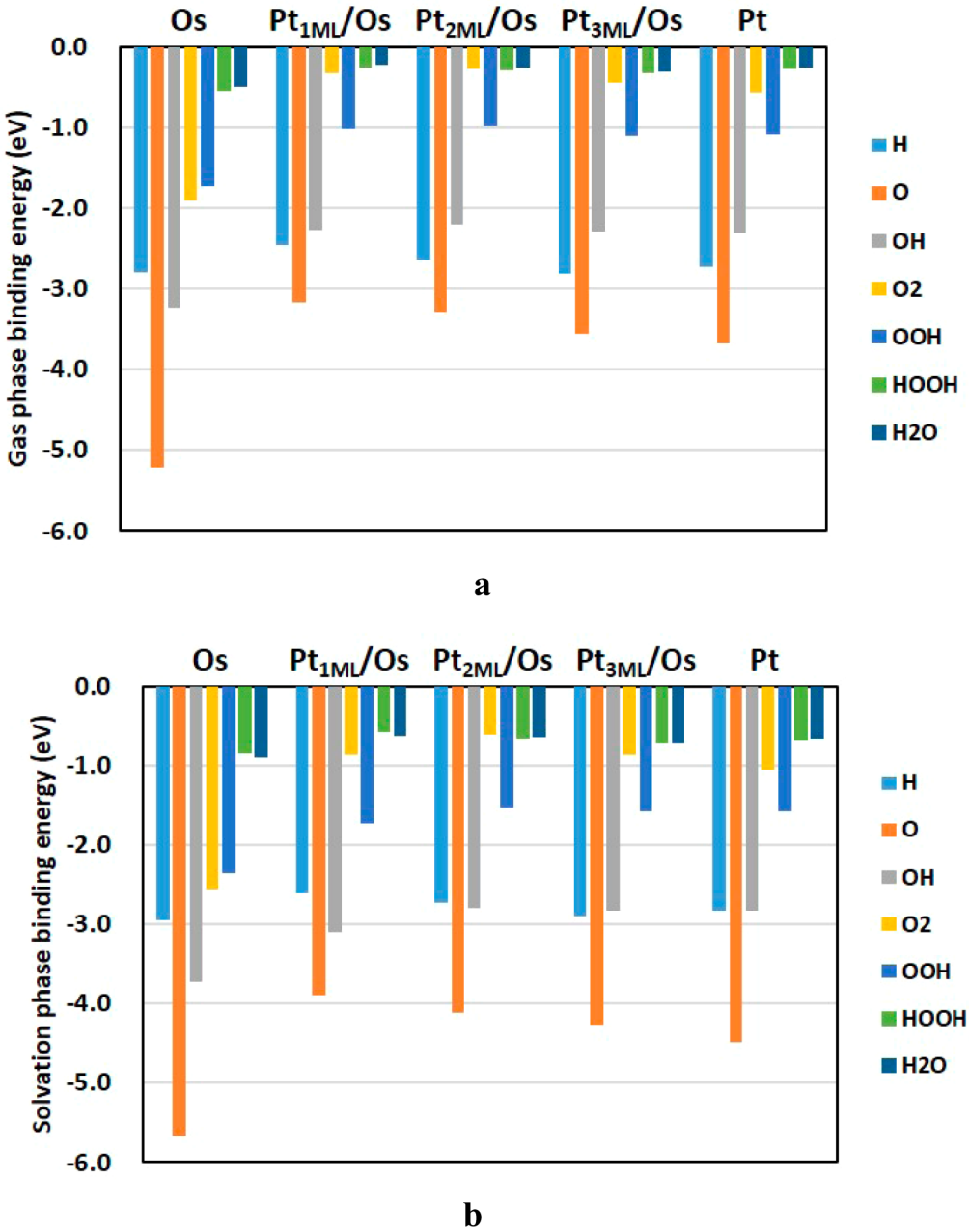

Figure 4. Binding energies of the ORR intermediates at the most stable sites on Os, Pt, and Pt/Os surfaces in gas phase (a) and solution (b).

3.3. Reaction Energy Barriers. On the basis of our previously obtained results,[37,89,94] the ORR could be divided into three fundamental stages:

I. $O_2 \rightarrow O$: dissociation of O_2 to become O, which could be either via direct O_2 dissociation: $O_2 \rightarrow 2O$ or OOH dissociation: $OOH \rightarrow O+OH$ following OOH formation: $O_2+H \rightarrow OOH$
II. $O \rightarrow OH$: OH formation. This step could be OH formation, O hydration, or H-OOH dissociation: $O+H \rightarrow OH$, $O+H_2O \rightarrow 2OH$, $H+OOH \rightarrow 2OH$
III. $OH \rightarrow H_2O$: H_2O formation from OH generated in the second stage: $OH+H \rightarrow H_2O$

Here we consider the reactions which proceed via the Langmuir–Hinshelwood mechanism. According to our previous result, the estimated energy barrier for a hydronium ion adsorbed on the Pt surface is 0.25 eV,[94] which is consistent with other published results[95,96] and lower than the RDS barrier for pure Pt, 0.50 eV (0.37 eV, if the H-OOH-diss mechanism is realized for Pt). A coadsorbed hydronium ion with anions have also been observed experimentally at potential higher than 0.6 V (RHE).[97] Figure 5 shows the ORR pathway and potential energy surface for Os, Pt, and Os/Pt core–shell catalysts in gas phase. The reaction energy barriers for each ORR step in gas phase are listed in Table S4.

In stage I, the O_2 dissociation energy barrier is higher than the OOH formation/dissociation barriers for the Pt and Os/Pt core–shell catalysts. Thus, it is more difficult for the ORR to start from the direct O_2 dissociation, but for Os, this step is favorable. This is due to the stronger O binding on the Os surface which prompts direct O_2 dissociation.

In stage II, the direct OH formation step has a much higher barrier which makes the oxygen hydration reaction and H-

DOI: 10.1021/cs501020a
ACS Catal. 2015, 5, 1568–1580

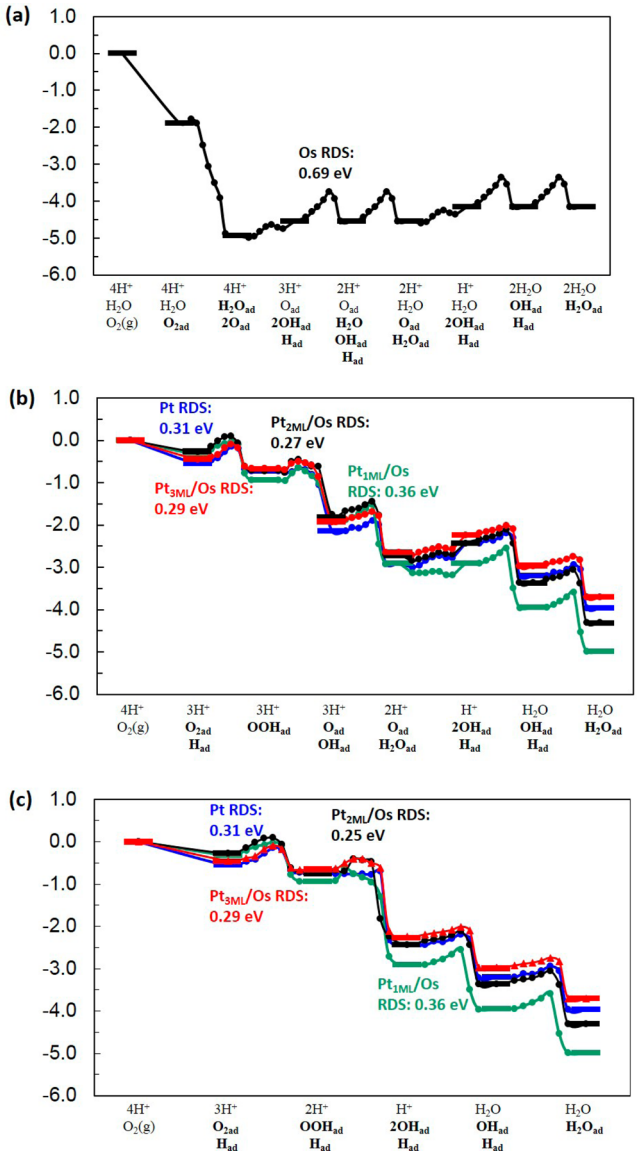

Figure 5. Potential energy surface including reaction barriers for the O_2-diss-hydr mechanism for Os (a), OOH-form-hydr mechanism (b), and H-OOH-diss mechanism (c) for Pt and Pt/Os catalysts in gas phase.

OOH dissociation more feasible, because the reaction proceeds along the lowest energy path.

In stage III, we find that the H_2O formation reaction energy barrier decreases, while the OOH formation energy barrier increases, with the increasing number of deposited Pt layers. Thus, the RDS is a compromise between the OOH formation reaction (stage I) with the energy barrier from 0.18 to 0.31 eV and the H_2O formation reaction (stage III) with the energy barrier from 0.19 to 0.36 eV for the Pt and Os/Pt catalysts in gas phase. For pure Os, the O_2 dissociation is barrierless, but the H_2O formation has a barrier of 0.69 eV, much higher than the corresponding values for the Pt or Os/Pt catalysts. This is because of the much stronger OH binding which makes difficult the H_2O formation reaction. Therefore, the RDS for pure Os is the H_2O formation reaction.

The ORR potential energy surface and reaction barriers in solution are shown in Figure 6 and listed in Table S5. Although the O_2 dissociation barriers are greatly reduced due to the

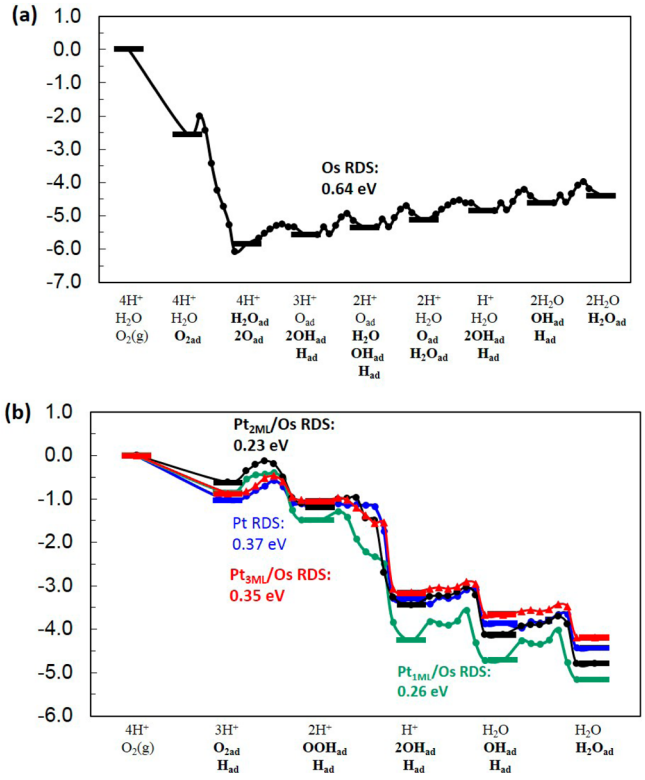

Figure 6. Potential energy surface including reaction barriers for the O_2-diss-hydr mechanism for Os (a) and H-OOH-diss mechanism (b) for Pt and Pt/Os catalysts in solution.

solvent effect, the O_2 dissociation reaction and oxygen hydration reaction barriers show opposite trends versus the increasing number of deposited Pt layers. This occurs because the O binding energy in the solvent rises as the number of deposited Pt layers increases. The lower O binding energy benefits the O_2 dissociation reaction but hinders the O hydration reaction. Similar phenomena have been reported for pure metals in stage I and III.[98] The reaction energy barriers for the direct O_2 dissociation followed by the oxygen hydration reaction are higher than the barriers for the path starting from the OOH formation reaction and followed by the H-OOH dissociation reaction. Thus, the reaction path via the OOH formation is favorable for pure Pt and Os/Pt catalysts, which is in agreement with results obtained by other groups[13,95] proposing a similar ORR mechanism for Pt. The RDS barrier is again a compromise between stage I and stage III (see Figure S1).

For pure Os, the OOH formation barrier is much higher because of the stronger O_2 binding. Thus, the ORR proceeds through the direct O_2 dissociation and then the O hydration reaction. The RDS is 0.64 eV for Os, while for pure Pt, Pt_{1ML}/Os, Pt_{2ML}/Os, and Pt_{3ML}/Os, the RDS is 0.37, 0.26, 0.23, and 0.35 eV, respectively. Therefore, we may expect that the ORR catalytic activity obeys the following trend: Pt_{2ML}/Os > Pt_{1ML}/Os > Pt_{3ML}/Os> Pt > Os, which allows us to consider the Os/Pt core−shell materials as potential candidates for the ORR catalysts.

Although we do not consider here the influence of the electrode potential on the ORR in detail, we have briefly analyzed the thermodynamic effect of the electrode potential by examining the Eley−Rideal mechanism. For this, we applied the approach developed by Norskøv et al.[99−101] In this approach,

DOI: 10.1021/cs501020a
ACS Catal. 2015, 5, 1568−1580

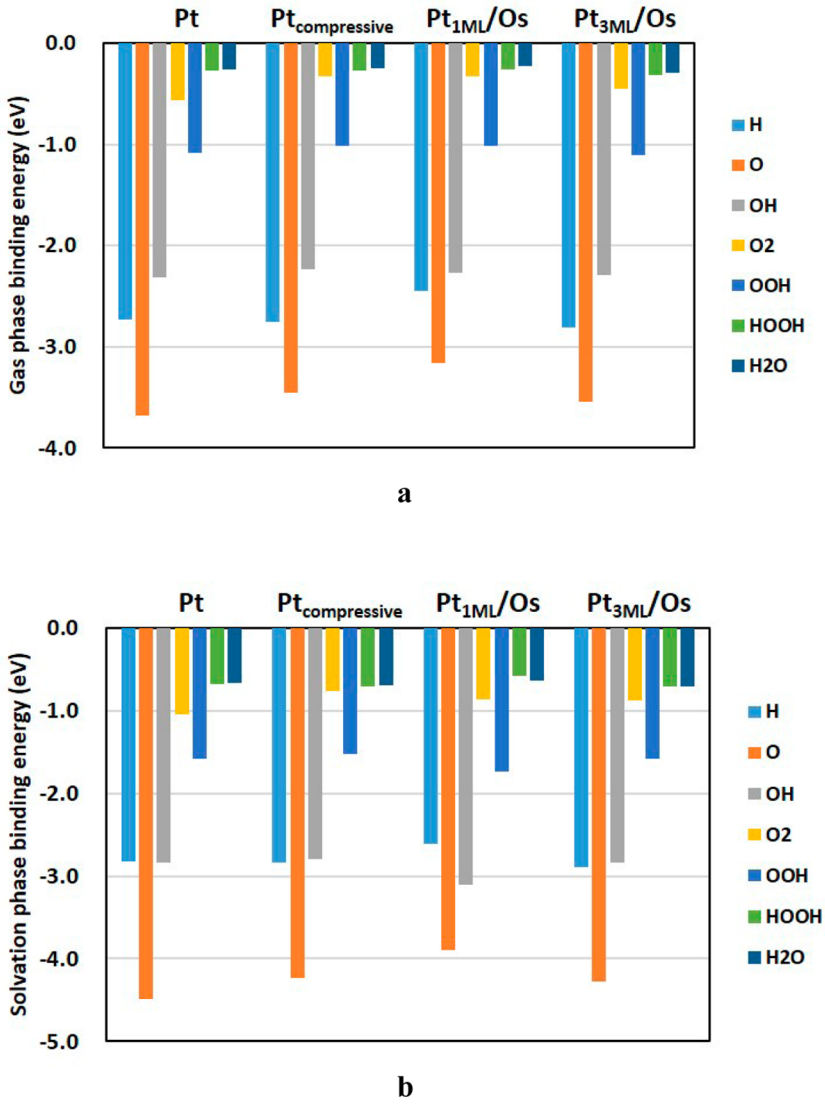

Figure 7. Binding energies of ORR species for Pt, compressive Pt, and Pt/Os surfaces in gas phase (a) and solution (b).

the reaction energy barriers are not considered properly but are assumed to be equal at least to the energy differences of the corresponding endothermic reactions, whereas the exothermic reactions are regarded as spontaneous and barrierless. The ORR potential energy surfaces for the Eley–Rideal reactions in solution are shown for the O_2-diss-hydr and H-OOH-diss mechanisms in Figures S2 and S3, respectively. The ORR pathways obtained for the Os, Pt, and Pt/Os surfaces using the Eley–Rideal mechanism are consistent with those resulting from the Langmuir–Hinshelwood mechanism. On the Os surface, the O_2-diss-hydr mechanism is preferable, whereas on the Pt and Pt/Os surfaces, the H-OOH-diss mechanism dominates. At potential lower than 0.80 V, the ORR is almost barrierless for the Pt/Os catalysts with a slightly higher barrier for pure Pt (0.17 eV at 0.80 V). At 1.23 V, the RDS for Pt_{1ML}/Os is the H_2O formation reaction with a barrier of 0.45 eV, while for Pt_{2ML}/Os, Pt_{3ML}/Os, and Pt, the RDS is the OOH formation reaction with a barrier of 0.23, 0.42 and 0.60 eV, respectively. The RDS is again a compromise between the H_2O formation and OOH-formation reactions and Pt_{2ML}/Os is the best among the catalysts considered here.

Overall, we can say that the result obtained for the Eley–Rideal mechanism generally agrees with that obtained for the Langmuir–Hinshelwood mechanism and does not affect our conclusions.

3.4. Strain and Ligand Effects. There are many publications, both experimental and theoretical (see, for instance, refs 102–104), that discuss the strain and ligand effects for the heteroepitaxial metal layers (bimetallic overlayers). The strain effect arises due to the bond length difference between the deposited layers and the substrate, whereas the ligand effect describes the effect owing to the heterometallic bonding between the surface atoms and the substrate atoms, which changes the electronic structure.

To study the strain effect, we compress the Pt bond lengths to the Os bond length value and compare the binding energies of different ORR species and reaction barriers for Pt and Pt_{3ML}/Os. Figure 7 compares the binding energies of the ORR species on the pure Pt, compressive Pt, Pt_{1ML}/Os, and Pt_{3ML}/Os surfaces in gas phase and solution (the corresponding values are listed in Tables S6 and S7, respectively). In both phases, all binding energies for Pt_{3ML}/Os are similar to those for compressive Pt, which include the strain effect but exclude

DOI: 10.1021/cs501020a
ACS Catal. 2015, 5, 1568–1580

the ligand effect. On the other hand, the binding energy differences between compressive Pt and Pt_{1ML}/Os are larger. This phenomenon is more obvious in solvation phase than in gas phase.

Because the ligand effect decreases with respect to the increasing number of deposited Pt layers, the ligand effect is more significant in Pt_{1ML}/Os than in Pt_{3ML}/Os. This result supports the viewpoint that the ligand effect of the Os substrate plays an important role. A similar conclusion could be made from the reaction energy barriers (Figure 8, Tables S8 and S9).

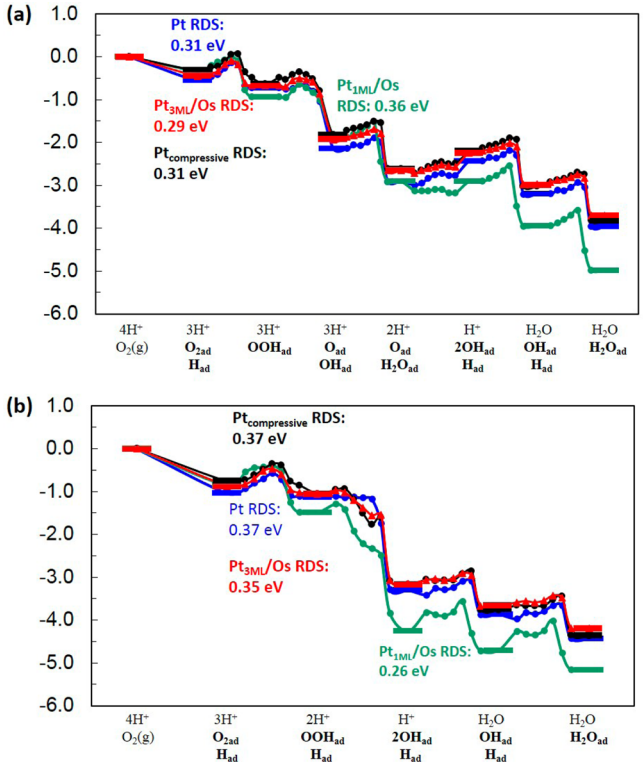

Figure 8. Potential energy surface including reaction barriers of H-OOH-diss-hydr mechanism for Pt, compressive Pt, and Pt/Os catalysts in gas phase (a) and solution (b).

The barrier differences between pure Pt, Pt_{3ML}/Os, and compressive Pt are lower than the differences between Pt_{1ML}/Os and compressive Pt. This implies that the ligand effect of the Os substrate is responsible for the improved ORR catalytic activity, rather than the strain effect. The RDS barrier becomes higher and approaches the value for pure Pt with the increasing number of deposited Pt layers (see Table S5). Previously, it had been explained by weakening of the ligand effect, when the number of deposited Pt layers increases.[103]

The ligand effect can be seen in Figure 7, Tables S6 and S7. We find that Pt_{3ML}/Os, which experiences a weaker ligand effect than Pt_{1ML}/Os, has similar binding energy values with compressive Pt. In general, the ligand effect, as well as the strain effect, weakens the ORR species binding on the Os/Pt core–shell structure compared to pure Pt. However, too weak binding of certain ORR intermediates may result in a higher barrier for the critical reaction. That is why Pt_{2ML}/Os, which has a binding energy closer to the optimal value than Pt_{1ML}/Os, shows better ORR activity than Pt_{1ML}/Os (see Figure S1, which shows a compromise between the OOH formation and H_2O formation steps).

3.5. Experimental Results. XRD pattern of Os/C and standard Os in the hcp phase (JCPDS: 006-0662) shows diffraction signals at 38.1°, 43.2°, 57.5°, 68.5°, and 77.4°, and their corresponding diffraction planes were identified clearly (see Figure S4). These diffraction signals exhibited typical peak-broadening because of the finite Os particle size. Using the Debye–Scherrer equation on the (012) diffraction peak, we estimated the average Os nanoparticle size to be 3.28 nm. It should be noted that the XRD patterns of $Pt_{1ML}/Os/C$ and $Pt_{2ML}/Os/C$ are identical because the effect of Pt was negligible, since the Pt atoms only occupy the shell layer in less than 2 atomic layer thickness.

A HAADF STEM image for the $Pt_{2ML}/Os/C$ particle is shown in Figure 9a. Although the HAADF technique could supply clear contrast for interface/locations because of various elements distribution,[32] some HAADF STEM images do not show clear core–shell structure contrast, like in our case, where the atomic number variation (Z contrast) is not significant, as discussed previously.[32,105,106] Figure 9b shows the element profile analysis for a $Pt_{2ML}/Os/C$ nanoparticle from the STEM-EDS measurement with a probe size of about 1.5 Å. As shown, $Pt_{2ML}/Os/C$ revealed a core–shell structure in which the core consisted of Os atoms and the shell was predominately occupied by the Pt atoms.

Figure 10 shows the CV curves of Os/C, $Pt_{1ML}/Os/C$, $Pt_{2ML}/Os/C$, and Pt/C for ECSA determination by hydrogen adsorption. The ECSA values for Pt/C, $Pt_{1ML}/Os/C$, and $Pt_{2ML}/Os/C$ were 2.39, 1.18, and 1.88 cm_{Pt}^2, respectively. The Pt/Os/C catalysts and pure Pt have different adsorption behavior, because the modified structure weakens the

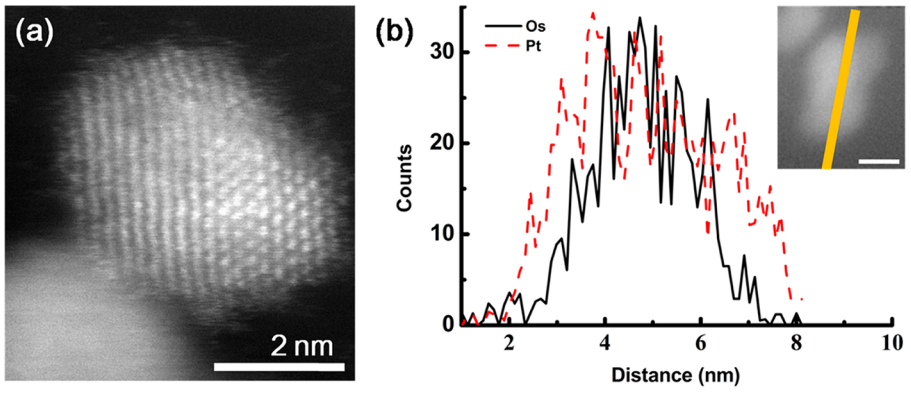

Figure 9. HAADF STEM image (a) and EDS line-scan (b) of a $Pt_{2ML}/Os/C$ nanoparticle.

DOI: 10.1021/cs501020a
ACS Catal. 2015, 5, 1568–1580

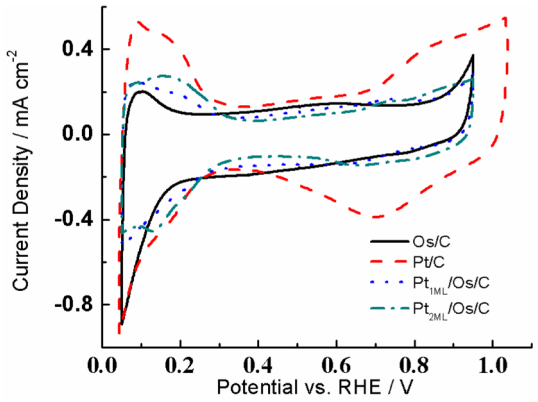

Figure 10. CV curves for ECSA determination for Os/C, Pt/C, Pt_{1ML}/Os/C and Pt_{2ML}/Os/C, respectively. The electrolyte was deaerated 0.1 M aqueous $HClO_4$.

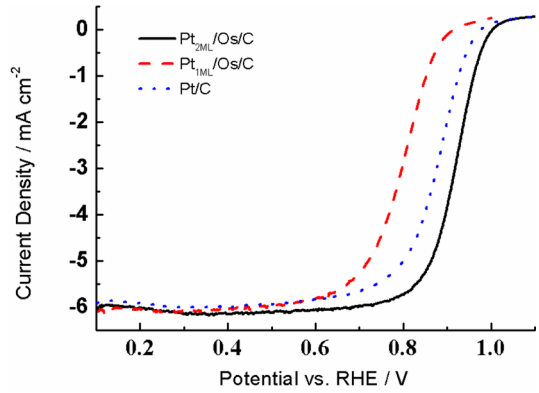

Figure 11. ORR curves of Pt/C, Pt_{1ML}/Os/C, and Pt_{2ML}/Os/C in apparent current density. The electrolyte was oxygen-saturated 0.1 M aqueous $HClO_4$ solution, and the scan rate was 20 mV/s.

interaction between adsorbates and catalyst surfaces,[107] which can also be seen in Tables S2 and S3. By increasing the thickness of Pt overlayer, the current densities at the double layer region (0.3−0.6 V vs RHE) are decreased (see Figure S5). The increased current densities at the double layer region of Pt_{1ML}/Os/C is possibly due to the oxidation of incompletely covered Os, similar to the Ru/Pt catalyst.[39] Therefore, we reasonably concluded that the Pt in Pt_{1ML}/Os/C did not cover the entire Os surface, but in the case of Pt_{2ML}/Os/C, the surface was more completely covered by the Pt atoms. This is anticipated because even in a straightforward displacement reaction process, the stoichiometric ratio of Cu/Pt was 1:1, and previous literature reported that the galvanic displacement did not form a continuous layer but a fine structure with some nanovoids or 2 ML deposits in some spots,[72] or the deposit formed by interconnected Pt islands with some holes.[74,108] A similar 3D island structure was also observed by using the extended X-ray adsorption fine structure (EXAFS) analysis applied for Pt/Rh(0001)[41] and Au/Pd[109] samples which were prepared via the Cu UPD displacement process. The island structure formation might be due to the incomplete Cu UPD shell structure before galvanic displacement.[110] Furthermore, some references reported that Cl^-, as a strong complexing ligand, promotes the stability of Cu(I) over than Cu(II)[111,112] which make the stoichiometric ratio greater than one. Therefore, the Os bare surface of the Pt_{1ML}/Os/C catalyst is not fully covered by the Pt deposit, but the Pt_{2ML}/Os/C has much better Pt coverage. The incomplete coverage decreases the stability of the Pt/Os/C catalysts. However, in our previous publication about dealloyed PtOs nanocatalysts,[68] we reported that the stability of dealloyed PtOs nanoparticles after 10 000 CV cycles was better than that of pure Pt. This implies that with complete Pt coverage, which could be reached by using another technique, Pt/Os core−shell catalysts may have a good enough stability.

Figure 11 demonstrates the ORR CV curves in apparent current density for Pt_{1ML}/Os/C, Pt_{2ML}/Os/C, and Pt/C. At potential below 0.6 V, the ORR response is under mass transport control limited by the diffusion of the dissolved oxygen in the electrolyte, whereas at potential between 0.8 and 1 V, the ORR response is dominated by kinetics (the electrocatalytic activity of the electrocatalyst involved in the ORR process).[113] Hence, a simple method to quickly evaluate the ORR behavior of a potential electrocatalyst is the reading of half-wave potential, which is defined as the potential at which the magnitude of the current is half of the limiting current. In general, the larger the half-wave potential, the greater the ORR activity. As shown, the half-wave potentials for the Pt/C, Pt_{1ML}/Os/C, and Pt_{2ML}/Os/C were 876, 795, and 918 mV, respectively. It should be noted that the diffusion-limiting current for these samples at a rotation speed of 1600 rpm was close to 6 mA cm^{-2}, which is consistent with the value earlier reported.[114] This consistence indicated that our ORR experiments were carried out properly.

To extract the kinetic information, we employed the Kouteck-Levich equation listed below

$$1/i = 1/i_{\text{kinetic}} + 1/i_{\text{diffusion limit}} = 1/i_{\text{kinetic}} + 1/0.62nFAD_{O2}{}^{2/3}\omega^{1/2}\nu^{-1/6}C_{O2}$$

where i is the experimentally measured current, $i_{\text{diffusion limit}}$ is the diffusion-limiting current due to the limitation of mass transport of dissolved oxygen in the 0.1 M aqueous $HClO_4$ solution, i_{kinetic} is the kinetic current associated with the ORR activity, n is the number of electron transferred in the ORR process (4, in our case), F is the Faraday constant, A is the reaction area of the RDE (0.196 cm^2), D_{O2} is the diffusivity of dissolved oxygen in the 0.1 M aqueous $HClO_4$ solution (1.93×10^{-5} cm^2 s^{-1}), ω is the rotation speed of the RDE, ν is the kinematic viscosity of the 0.1 M aqueous $HClO_4$ solution (1.009×10^{-2} cm^2 s^{-1}), and C_{O2} is the concentration of dissolved oxygen in the 0.1 M aqueous $HClO_4$ solution (1.26×10^{-3} mol L^{-1}).[115] The respective kinetic parameters are listed in Table 2. As it was mentioned above, the Os core of Pt_{1ML}/Os/C is not fully covered by Pt atoms. According to our solvation calculation (Table S5), the ORR at the Os surface is very sluggish because of the high H_2O formation reaction energy barrier due to the strong OH binding. This causes the catalytic performance of Pt_{1ML}/Os/C, which is not completely covered by Pt, to be even worse than that of the commercial Pt catalyst. The Pt_{2ML}/Os/C sample, which is more completely covered by Pt atoms and shows a core−shell structure, exhibits excellent catalytic activity. It is in agreement with the low reaction energy barriers for the Pt_{1ML}/Os and Pt_{2ML}/Os catalysts (Table S5) from our computational evaluations. Relationships between the experimental half wave potential and theoretical OH binding energy and RDS barriers in solution are shown in Figures S6 and S7, respectively. Indeed, Pt_{2ML}/Os/C shows 3.5 times better mass activity, when considering only Pt loading, and 5 times better specific activity

DOI: 10.1021/cs501020a
ACS Catal. 2015, 5, 1568−1580

Table 2. Comparison of Kinetic Data for ORR Os/Pt Core-Shell Catalysts

catalyst	Pt loading (μg)	I_{mass} (mA μg_{Pt}^{-1})	I_{mass} (mA μg_{Pt+Os}^{-1})	$i_{specific}$ (mA cm_{Pt}^{-2})	half-wave potential (V vs RHE)
Pt/C	3	−0.20	−0.20	−0.26	0.876
Pt_{1ML}/Os/C	1.42	0	0	0	0.795
Pt_{2ML}/Os/C	2.82	−0.70	−0.45	−1.33	0.918

for ORR compared to those of Pt/C (Table 2 and Figure S8). Considering a total precious metal loading (Pt + Os), Pt_{2ML}/Os/C shows over 2 times better activity (Figure S8).

4. CONCLUSION

We applied both QM calculations and electrochemical measurements to evaluate the catalytic activity of the Pt/Os/C catalysts. Using QM calculations, we identified the most stable structures for various layer Pt deposits on the Os substrate, and these structures were applied to calculate binding energies and reaction energy barriers for the ORR species. In general, the binding energy increases with the number of Pt deposit layers and approaches the values on the pure Pt surface both in gas phase and solution. This result confirms that the ligand effect gradually decreases as the number of Pt deposit layers increases. The calculated RDS barriers predict the ORR catalytic activity as following: Pt_{2ML}/Os > Pt_{1ML}/Os > Pt_{3ML}/Os > Pt > Os. To further understand the origin of the higher catalytic activity of the Pt/Os surfaces, a nonphysical compressive Pt system was built to compare its reaction energy barriers and binding energies to Pt, Pt_{1ML}/Os and Pt_{3ML}/Os. The results implied that due to changes in the electronic structure of the Pt/Os catalysts, the ligand effect might be more important for the improved ORR activity than the purely compressive strain effect.

Pt/Os/C catalysts were fabricated by the chemical synthesis and UPD method. XRD and TEM technologies were applied for materials characterization. The CV curves for Os, Pt_{1ML}/Os/C, and Pt showed that in Pt_{1ML}/Os/C, the Os substrate is only partially covered by Pt atoms. The more complete Pt coverage is formed after the second UPD process. The SEM-EDS analysis proved the existence of the core−shell structure for our Pt_{2ML}/Os/C catalyst. The ORR CV curves demonstrate that the Pt_{2ML}/Os/C structure shows 3.5 to 5 times better catalytic activity than Pt/C, which allows the Os/Pt core−shell structured materials to be considered as a potential ORR catalyst. The experimentally observed ORR catalytic activity follows the sequence: Pt_{2ML}/Os/C > Pt/C > Pt_{1ML}/Os/C, which agrees with our theoretical prediction, based on the ORR energy barrier calculations.

■ ASSOCIATED CONTENT

Supporting Information

The following file is available free of charge on the ACS Publications website at DOI: 10.1021/cs501020a.

Figures on the barriers for the OOH formation and H_2O formation reactions, potential energy surfaces for the O_2-diss-hydr and H-OOH-diss ORR mechanisms in solution, XRD patterns,, CV curves; correlations between experimental half wave potential, OH binding energy, and RDS barriers; mass and specific activities of Pt/C and Pt_{2ML}/Os/C at 0.9 V; tables with calculated surface segregation energies for Pt_3X alloys; binding energies and ORR barriers for Os, Pt, and Pt/Os catalysts (PDF)

■ AUTHOR INFORMATION

Corresponding Authors

*E-mail: merinov@caltech.edu (B.V.M.).
*E-mail: wag@wag.caltech.edu (W.A.G.).

Notes

The authors declare no competing financial interest.

■ ACKNOWLEDGMENTS

This work was supported by Caltech and Taiwan Energy Exchange (CTEE) collaborative program funded by the National Science Council of Taiwan (grant NSC 103-3113-P-008-001) and partially by the National Science Foundation (grant CBET-1067848, Caltech). The work performed at Brookhaven National Laboratory was supported by the U.S. Department of Energy under contract DE-AC02-98CH10886. The facilities of the Materials and Process Simulation Center used in this study were established with grants from DURIP-ONR, DURIP-ARO, and NSF-CSEM.

■ REFERENCES

(1) Borup, R.; Meyers, J.; Pivovar, B.; Kim, Y. S.; Mukundan, R.; Garland, N.; Myers, D.; Wilson, M.; Garzon, F.; Wood, D.; Zelenay, P.; More, K.; Stroh, K.; Zawodzinski, T.; Boncella, J.; McGrath, J. E.; Inaba, M.; Miyatake, K.; Hori, M.; Ota, K.; Ogumi, Z.; Miyata, S.; Nishikata, A.; Siroma, Z.; Uchimoto, Y.; Yasuda, K.; Kimijima, K. I.; Iwashita, N. *Chem. Rev.* **2007**, *107*, 3904−3951.
(2) Wang, Y.; Chen, K. S.; Mishler, J.; Cho, S. C.; Adroher, X. C. *Appl. Energy* **2011**, *88*, 981−1007.
(3) Yasuda, K.; Taniguchi, A.; Akita, T.; Ioroi, T.; Siroma, Z. *Phys. Chem. Chem. Phys.* **2006**, *8*, 746−752.
(4) Eroglu, M.; Dursun, E.; Sevencan, S.; Song, J.; Yazici, S.; Kilic, O. *Int. J. Hydrogen Energy* **2011**, *36*, 7985−7992.
(5) Steele, B. C. H.; Heinzel, A. *Nature* **2001**, *414*, 345−352.
(6) Kordesch, K.; Simader, G. *Fuel Cells and Their Applications*; Wiley-VCH: New York, 1996.
(7) Appleby, A. J.; Foulkes, F. R. *Fuel Cell Handbook*; Van Nostrand Reinhold: New York, 1989.
(8) O'Hayre, R. P.; Cha, S. W.; Colella, W.; Prinz, F. B. *Fuel Cell Fundamentals*; 2nd ed.; John Wiley and Sons: New York, 2006.
(9) Hammer, B.; Nørskov, J. K. *Adv. Catal.* **2000**, *45*, 71−129.
(10) Xin, H.; Holewinski, A.; Schweitzer, N.; Nikolla, E.; Linic, S. *Top. Catal.* **2012**, *55*, 376−390.
(11) Xin, H.; Holewinski, A.; Linic, S. *ACS Catal.* **2011**, *2*, 12−16.
(12) Holewinski, A.; Linic, S. *J. Electrochem. Soc.* **2012**, *159*, H864−H870.
(13) Wei, G. F.; Fang, Y. H.; Liu, Z. P. *J. Phys. Chem. C* **2012**, *116*, 12696−12705.
(14) Fang, Y. H.; Liu, Z. P. *J. Phys. Chem. C* **2011**, *115*, 17508−17515.
(15) Wei, G. F.; Liu, Z. P. *Phys. Chem. Chem. Phys.* **2013**, *15*, 18555−18561.
(16) Jacob, T.; Goddard, W. A. *ChemPhysChem* **2006**, *7*, 992−1005.
(17) Keith, J. A.; Jerkiewicz, G.; Jacob, T. *ChemPhysChem* **2010**, *11*, 2779−2794.
(18) Wang, B. *J. Power Sources* **2005**, *152*, 1−15.
(19) Bashyam, R.; Zelenay, P. *Nature* **2006**, *443*, 63−66.
(20) Othman, R.; Dicks, A. L.; Zhu, Z. *Int. J. Hydrogen Energy* **2012**, *37*, 357−372.
(21) Debe, M. K. *Nature* **2012**, *486*, 43−51.

DOI: 10.1021/cs501020a
ACS Catal. 2015, 5, 1568−1580

(22) Yang, H. *Angew. Chem., Int. Ed.* **2011**, *50*, 2674−2676.
(23) Stamenkovic, V.; Mun, B. S.; Mayrhofer, K. J. J.; Ross, P. N.; Markovic, N. M.; Rossmeisl, J.; Greeley, J.; Nørskov, J. K. *Angew. Chem.* **2006**, *118*, 2963−2967.
(24) Nilekar, A. U.; Xu, Y.; Zhang, J.; Vukmirovic, M. B.; Sasaki, K.; Adzic, R. R.; Mavrikakis, M. *Top. Catal.* **2007**, *46*, 276−284.
(25) Stamenkovic, V. R.; Fowler, B.; Mun, B. S.; Wang, G.; Ross, P. N.; Lucas, C. A.; Markovic, N. M. *Science* **2007**, *315*, 493−497.
(26) Adzic, R. R.; Zhang, J.; Sasaki, K.; Vukmirovic, M. B.; Shao, M.; Wang, J. X.; Nilekar, A. U.; Mavrikakis, M.; Valerio, J. A.; Uribe, F. *Top. Catal.* **2007**, *46*, 249−262.
(27) Stamenkovic, V. R.; Mun, B. S.; Arenz, M.; Mayrhofer, K. J.; Lucas, C. A.; Wang, G.; Ross, P. N.; Markovic, N. M. *Nat. Mater.* **2007**, *6*, 241−247.
(28) Greeley, J.; Stephens, I. E. L.; Bondarenko, A. S.; Johansson, T. P.; Hansen, H. A.; Jaramillo, T. F.; Rossmeisl, J.; Chorkendorff, I.; Nørskov, J. K. *Nat. Chem.* **2009**, *1*, 552−556.
(29) Zhou, W. P.; Yang, X. F.; Vukmirovic, M. B.; Koel, B. E.; Jiao, J.; Peng, G. W.; Mavrikakis, M.; Adzic, R. R. *J. Am. Chem. Soc.* **2009**, *131*, 12755−12762.
(30) Wang, J. X.; Inada, H.; Wu, L. J.; Zhu, Y. M.; Choi, Y. M.; Liu, P.; Zhou, W. P.; Adzic, R. R. *J. Am. Chem. Soc.* **2009**, *131*, 17298−17302.
(31) Gong, K. P.; Su, D.; Adzic, R. R. *J. Am. Chem. Soc.* **2010**, *132*, 14364−14366.
(32) Sasaki, K.; Wang, J. X.; Naohara, H.; Marinkovic, N.; More, K.; Inada, H.; Adzic, R. R. *Electrochim. Acta* **2010**, *55*, 2645−2652.
(33) Knupp, S. L.; Vukmirovic, M. B.; Haldar, P.; Herron, J. A.; Mavrikakis, M.; Adzic, R. R. *Electrocatal.* **2010**, *1*, 213−223.
(34) Sasaki, K.; Naohara, H.; Cai, Y.; Choi, Y. M.; Liu, P.; Vukmirovic, M. B.; Wang, J. X.; Adzic, R. R. *Angew. Chem., Int. Ed. Engl.* **2010**, *49*, 8602−8607.
(35) Bing, Y.; Liu, H.; Zhang, L.; Ghosh, D.; Zhang, J. *Chem. Soc. Rev.* **2010**, *39*, 2184−2202.
(36) Yu, T. H.; Sha, Y.; Merinov, B. V.; Goddard, W. A. *J. Phys. Chem. C* **2010**, *114*, 11527−11533.
(37) Sha, Y.; Yu, T. H.; Merinov, B. V.; Shirvanian, P.; Goddard, W. A., III *J. Phys. Chem. C* **2012**, *116*, 21334−21342.
(38) Adzic, R. R. *Electrocatal.* **2012**, *3*, 163−169.
(39) Yang, L.; Vukmirovic, M. B.; Su, D.; Sasaki, K.; Herron, J. A.; Mavrikakis, M.; Liao, S.; Adzic, R. R. *J. Phys. Chem. C* **2013**, *117*, 1748−1753.
(40) Brimaud, S.; Engstfeld, A.; Alves, O.; Hoster, H.; Behm, R. *Top. Catal.* **2014**, *57*, 222−235.
(41) Friebel, D.; Viswanathan, V.; Miller, D. J.; Anniyev, T.; Ogasawara, H.; Larsen, A. H.; O'Grady, C. P.; Nørskov, J. K.; Nilsson, A. *J. Am. Chem. Soc.* **2012**, *134*, 9664−9671.
(42) Jackson, A.; Viswanathan, V.; Forman, A. J.; Larsen, A. H.; Nørskov, J. K.; Jaramillo, T. F. *ChemElectroChem.* **2014**, *1*, 67−71.
(43) Colón-Mercado, H. R.; Popov, B. N. *J. Power Sources* **2006**, *155*, 253−263.
(44) Colón-Mercado, H. R.; Kim, H.; Popov, B. N. *Electrochem. Commun.* **2004**, *6*, 795−799.
(45) Maillard, F.; Dubau, L.; Durst, J.; Chatenet, M.; André, J.; Rossinot, E. *Electrochem. Commun.* **2010**, *12*, 1161−1164.
(46) Chen, S.; Ferreira, P. J.; Sheng, W. C.; Yabuuchi, N.; Allard, L. F.; Shao-Horn, Y. *J. Am. Chem. Soc.* **2008**, *130*, 13818−13819.
(47) Watanabe, M.; Tsurumi, K.; Mizukami, T.; Nakamura, T.; Stonehart, P. *J. Electrochem. Soc.* **1994**, *141*, 2659−2668.
(48) Antolini, E.; Salgado, J. R. C.; Gonzalez, E. R. *J. Power Sources* **2006**, *160*, 957−968.
(49) Wakabayashi, N.; Takeichi, M.; Uchida, H.; Watanabe, M. *J. Phys. Chem. B* **2005**, *109*, 5836−5841.
(50) Ma, Y. G.; Balbuena, P. B. *Surf. Sci.* **2008**, *602*, 107−113.
(51) Chen, W.; Schneider, W. F.; Wolverton, C. *J. Phys. Chem. C* **2014**, *118*, 8342−8349.
(52) Tsai, H. C.; Yu, T. H.; Sha, Y.; Merinov, B. V.; Wu, P. W.; Chen, S. Y.; Goddard, W. A., III *J. Phys. Chem. C* **2014**, *118*, 26703−26712.
(53) Wei, G. F.; Liu, Z. P. *Energy Environ. Sci.* **2011**, *4*, 1268−1272.
(54) Mayrhofer, K. J.; Arenz, M. *Nat. Chem.* **2009**, *1*, 518−519.
(55) Hwang, S. J.; Kim, S. K.; Lee, J. G.; Lee, S. C.; Jang, J. H.; Kim, P.; Lim, T. H.; Sung, Y. E.; Yoo, S. J. *J. Am. Chem. Soc.* **2012**, *134*, 19508−19511.
(56) Dai, Y.; Ou, L.; Liang, W.; Yang, F.; Liu, Y.; Chen, S. *J. Phys. Chem. C* **2011**, *115*, 2162−2168.
(57) Brushett, F. R.; Duong, H. T.; Ng, J. W.; Behrens, R. L.; Wieckowski, A.; Kenis, P. J. A. *J. Electrochem. Soc.* **2010**, *157*, B837−B845.
(58) Nishimura, T.; Morikawa, T.; Yokoi, M.; Iwakura, C.; Inoue, H. *Electrochim. Acta* **2008**, *54*, 499−505.
(59) Johansson, T. P.; Ulrikkeholm, E. T.; Hernandez-Fernandez, P.; Malacrida, P.; Hansen, H. A.; Bandarenka, A. S.; Nørskov, J. K.; Rossmeisl, J.; Stephens, I. E. L.; Chorkendorff, I. *Top. Catal.* **2014**, *57*, 245−254.
(60) Ley, K. L.; Liu, R. X.; Pu, C.; Fan, Q. B.; Leyarovska, N.; Segre, C.; Smotkin, E. S. *J. Electrochem. Soc.* **1997**, *144*, 1543−1548.
(61) Kua, J.; Goddard, W. A., III *J. Am. Chem. Soc.* **1999**, *121*, 10928−10941.
(62) Gurau, B.; Viswanathan, R.; Liu, R. X.; Lafrenz, T. J.; Ley, K. L.; Smotkin, E. S.; Reddington, E.; Sapienza, A.; Chan, B. C.; Mallouk, T. E.; Sarangapani, S. *J. Phys. Chem. B* **1998**, *102*, 9997−10003.
(63) Crown, A.; Moraes, I. R.; Wieckowski, A. *J. Electroanal. Chem.* **2001**, *500*, 333−343.
(64) Huang, J. J.; Yang, H.; Huang, Q. H.; Tang, Y. W.; Lu, T. H.; Akins, D. L. *J. Electrochem. Soc.* **2004**, *151*, A1810−A1815.
(65) Santos, V. P.; Del Colle, V.; Bezerra, R. M.; Tremiliosi-Filho, G. *Electrochim. Acta* **2004**, *49*, 1221−1231.
(66) Liu, W.; Huang, J. *J. Power Sources* **2009**, *189*, 1012−1015.
(67) Zhang, J. L.; Vukmirovic, M. B.; Sasaki, K.; Nilekar, A. U.; Mavrikakis, M.; Adzic, R. R. *J. Am. Chem. Soc.* **2005**, *127*, 12480−12481.
(68) Lee, Y. J.; Hsieh, Y. C.; Tsai, H. C.; Lu, I. T.; Wu, Y. H.; Yu, T. H.; Merinov, B. V.; Goddard, W. A., III; Wu, P. W. *Appl. Catal., B* **2014**, *150−151*, 636−646.
(69) Fernandes, A. C.; Paganin, V. A.; Ticianelli, E. A. *J. Electroanal. Chem.* **2010**, *648*, 156−162.
(70) Chen, S.; Gasteiger, H. A.; Hayakawa, K.; Tada, T.; Shao-Horn, Y. *J. Electrochem. Soc.* **2010**, *157*, A82−A97.
(71) Ma, Y.; Balbuena, P. B. *Surf. Sci.* **2009**, *603*, 349−353.
(72) Brankovic, S. R.; Wang, J. X.; Adzic, R. R. *Surf. Sci.* **2001**, *474*, L173−L179.
(73) Herrero, E.; Buller, L. J.; Abruna, H. D. *Chem. Rev.* **2001**, *101*, 1897−1930.
(74) Zhang, J.; Mo, Y.; Vukmirovic, M. B.; Klie, R.; Sasaki, K.; Adzic, R. R. *J. Phys. Chem. B* **2004**, *108*, 10955−10964.
(75) Zhang, J.; Lima, F. H. B.; Shao, M. H.; Sasaki, K.; Wang, J. X.; Hanson, J.; Adzic, R. R. *J. Phys. Chem. B* **2005**, *109*, 22701−22704.
(76) Zhang, J.; Vukmirovic, M. B.; Xu, Y.; Mavrikakis, M.; Adzic, R. R. *Angew. Chem., Int. Ed. Engl.* **2005**, *44*, 2132−2135.
(77) Zhang, J.; Sasaki, K.; Sutter, E.; Adzic, R. R. *Science* **2007**, *315*, 220−222.
(78) Schultz, P. *SeqQuest, Electronic Structure Code*; Sandia National Laboratory: Albuquerque, NM. http://dft.sandia.gov/Quest/.
(79) Perdew, J. P.; Burke, K.; Ernzerhof, M. *Phys. Rev. Lett.* **1996**, *77*, 3865−3868.
(80) Ceperley, D. M.; Alder, B. J. *Phys. Rev. Lett.* **1980**, *45*, 566−569.
(81) Perdew, J. P.; Zunger, A. *Phys. Rev. B* **1981**, *23*, 5048−5079.
(82) Goddard, W. A., III *Phys. Rev.* **1968**, *174*, 659−662.
(83) Melius, C. F.; Goddard, W. A., III *Phys. Rev. A* **1974**, *10*, 1528−1540.
(84) Melius, C. F.; Olafson, B. D.; Goddard, W. A., III *Chem. Phys. Lett.* **1974**, *28*, 457−462.
(85) Redondo, A.; Goddard, W. A., III; McGill, T. C. *Phys. Rev. B* **1977**, *15*, 5038−5048.
(86) Hamann, D. R. *Phys. Rev. B* **1989**, *40*, 2980−2987.
(87) Mills, G.; Jonsson, H.; Schenter, G. K. *Surf. Sci.* **1995**, *324*, 305−337.
(88) Mills, G.; Jonsson, H. *Phys. Rev. Lett.* **1994**, *72*, 1124−1127.

DOI: 10.1021/cs501020a
ACS Catal. 2015, 5, 1568−1580

(89) Sha, Y.; Yu, T. H.; Liu, Y.; Merinov, B. V.; Goddard, W. A., III *J. Phys. Chem. Lett.* **2010**, *1*, 856−861.
(90) Holst, M.; Saied, F. *J. Comput. Chem.* **1993**, *14*, 105−113.
(91) Holst, M. J.; Saied, F. *J. Comput. Chem.* **1995**, *16*, 337−364.
(92) Baker, N. A.; Sept, D.; Joseph, S.; Holst, M. J.; McCammon, J. A. *Proc. Natl. Acad. Sci. U.S.A.* **2001**, *98*, 10037−10041.
(93) Hsieh, Y. C.; Zhang, Y.; Su, D.; Volkov, V.; Si, R.; Wu, L. J.; Zhu, Y. M.; An, W.; Liu, P.; He, P.; Ye, S. Y.; Adzic, R. R.; Wang, J. X. *Nat. Commun.* **2013**, *4*, Articleno. 2466.
(94) Sha, Y.; Yu, T. H.; Merinov, B. V.; Shirvanian, P.; Goddard, W. A., III *J. Phys. Chem. Lett.* **2011**, *2*, 572−576.
(95) Tripković, V.; Skúlason, E.; Siahrostami, S.; Nørskov, J. K.; Rossmeisl, J. *Electrochim. Acta* **2010**, *55*, 7975−7981.
(96) Anderson, A. B.; Sidik, R. A.; Narayanasamy, J.; Shiller, P. *J. Phys. Chem. B* **2003**, *107*, 4618−4623.
(97) Hirota, K.; Song, M. B.; Ito, M. *Chem. Phys. Lett.* **1996**, *250*, 335−341.
(98) Yu, T. H.; Hofmann, T.; Sha, Y.; Merinov, B. V.; Myers, D. J.; Heske, C.; Goddard, W. A., III *J. Phys. Chem. C* **2013**, *117*, 26598−26607.
(99) Nørskov, J. K.; Rossmeisl, J.; Logadottir, A.; Lindqvist, L.; Kitchin, J. R.; Bligaard, T.; Jonsson, H. *J. Phys. Chem. B* **2004**, *108*, 17886−17892.
(100) Karlberg, G.; Rossmeisl, J.; Nørskov, J. K. *Phys. Chem. Chem. Phys.* **2007**, *9*, 5158−5161.
(101) Viswanathan, V.; Hansen, H. A.; Rossmeisl, J.; Nørskov, J. K. *ACS Catal.* **2012**, *2*, 1654−1660.
(102) Mavrikakis, M.; Hammer, B.; Nørskov, J. K. *Phys. Rev. Lett.* **1998**, *81*, 2819−2822.
(103) Schlapka, A.; Lischka, M.; Groß, A.; Käsberger, U.; Jakob, P. *Phys. Rev. Lett.* **2003**, *91*, 016101.
(104) Kitchin, J. R.; Nørskov, J. K.; Barteau, M. A.; Chen, J. G. *Phys. Rev. Lett.* **2004**, *93*, 156801.
(105) Garcia-Gutierrez, D.; Gutierrez-Wing, C.; Miki-Yoshida, M.; Jose-Yacaman, M. *Appl. Phys. A-Mater.* **2004**, *79*, 481−487.
(106) Liu, C. P.; Twesten, R. D.; Gibson, J. M. *Ultramicroscopy* **2001**, *87*, 79−88.
(107) van der Vliet, D. F.; Wang, C.; Li, D.; Paulikas, A. P.; Greeley, J.; Rankin, R. B.; Strmcnik, D.; Tripkovic, D.; Markovic, N. M.; Stamenkovic, V. R. *Angew. Chem., Int. Ed.* **2012**, *51*, 3139−3142.
(108) Vukmirovic, M. B.; Bliznakov, S. T.; Sasaki, K.; Wang, J. X.; Adzic, R. R. *ECS Interface* **2011**, *20*, 33−40.
(109) Price, S. W.; Rhodes, J. M.; Calvillo, L.; Russell, A. E. *J. Phys. Chem. C* **2013**, *117*, 24858−24865.
(110) Price, S. W.; Speed, J. D.; Kannan, P.; Russell, A. E. *J. Am. Chem. Soc.* **2011**, *133*, 19448−19458.
(111) Gokcen, D.; Bae, S. E.; Brankovic, S. R. *J. Electrochem. Soc.* **2010**, *157*, D582−587.
(112) Lee, H. P.; Nobe, K. *J. Electrochem. Soc.* **1986**, *133*, 2035−2043.
(113) Paulus, U. A.; Schmidt, T. J.; Gasteiger, H. A.; Behm, R. J. *J. Electroanal. Chem.* **2001**, *495*, 134−145.
(114) Paulus, U. A.; Wokaun, A.; Scherer, G. G.; Schmidt, T. J.; Stamenkovic, V.; Radmilovic, V.; Markovic, N. M.; Ross, P. N. *J. Phys. Chem. B* **2002**, *106*, 4181−4191.
(115) Chen, S.; Sheng, W. C.; Yabuuchi, N.; Ferreira, P. J.; Allard, L. F.; Shao-Horn, Y. *J. Phys. Chem. C* **2009**, *113*, 1109−1125.

DOI: 10.1021/cs501020a
ACS Catal. 2015, 5, 1568−1580